





Simulation and lithographic fabrication of a triple band terahertz metamaterial absorber coated on flexible polyethylene terephthalate substrate

YADGAR I. ABDULKARIM,^{1,2}  MEIYU XIAO,³ HALGURD N. AWL,⁴ FAHMI F. MUHAMMADSHARIF,⁵ TINGTING LANG,³  SALAH RAZA SAEED,^{2,6} FATIH ÖZKAN ALKURT,⁷ MEHMET BAKIR,⁸ MUHARREM KARAASLAN,⁷ AND JIAN DONG^{1,*}

¹*School of Computer Science and Engineering, Central South University, Changsha 410075, China*

²*Medical Physics Department, College of Medicals & Applied Science, Charo University, 46023, Chamchamal, Sulaimania, Iraq*

³*Institute of Optoelectronic Technology, China Jiliang University, Hangzhou 310018, China*

⁴*Department of Communication Engineering, Sulaimani polytechnic University, Sulaimani, 46001, Iraq*

⁵*Department of Physics, Faculty of Science and Health, Koya University, 44023 Koya, Iraq*

⁶*Scientific Research and Development center, Nauroz University, 46001, Dhok, Iraq*

⁷*Department of Electrical-Electronics Engineering, Iskenderun Technical University, 31200 Hatay, Turkey*

⁸*Department of Computer Engineering, Bozok University, 66200 Yozgat, Turkey*

**dongjian@csu.edu.cn*

Abstract: A triple band metamaterial absorber in the terahertz range, incorporating a three closed circle ring resonator, was designed and fabricated on flexible polyethylene terephthalate “PET” substrate. The proposed design was investigated theoretically and experimentally. Computer simulation technology “CST” was used to study the designed structure, while lithography technique was used to fabricate the absorber and terahertz time-domain spectroscopy was utilized to measure the reflectivity. Results showed the presence of three intensive peaks at the resonance frequencies of ‘0.43, 0.61, and 0.88 THz’, which correspond to the absorptivity of 98%, 91%, and 98%, respectively. The sensitivity of the three peaks was found to be ‘70.5, 133, and 149.5 GHz/RIU’, respectively. The parametric studies and field distributions were analysed. Furthermore, the proposed design exhibited polarization insensitivity for both transverse electric “TE” and transverse magnetic “TM” modes from 00 to 900. It was concluded that the proposed design can be specifically viable for some important applications such as ‘THz’ images, filtering, biological sensing, and optical communications.

© 2021 Optica Publishing Group under the terms of the [Optica Open Access Publishing Agreement](#)

1. Introduction

The deep sub-wavelength structures known as metamaterials have attracted considerable attention due to their exotic properties not seen in nature such as negative constitutive parameters in microwave [1] or terahertz [2] frequency ranges. Thanks to these exotic behaviors, metamaterials can be interestingly used in various applications such as invisible cloaking [3,4], cross section reduction [5,6], performance enhancement of wireless communication systems [7], polarization conversions [8–10] and sensors [11,12]. In order to manipulate the incident electromagnetic waves, several approaches were reported including filtering [13,14], controlling [15] and absorbing the electromagnetic waves [16–18]. Recently, terahertz applications of metamaterial-based absorber structures were studied for light absorption applications [19,20]. In addition, the tunable band [21,22], dual band [23–26] and multiband [27–31] mechanism of terahertz absorbers was presented in literature.

The advantages of using terahertz frequency in an application is limitless and could be adapted to various fields such as imaging [32,33], medical [34,35], stealth [36] and sensing technologies [37,38]. Besides, researchers are mostly focused on the absorption applications in terahertz bands due to its wide range of working spectrum. In 2013, Hokmabadi et al. presented a quasi-static dynamic circuit model that describes the working principle of metamaterial absorbers in terahertz bands based on the “LC” resonance theory [39]. In addition, Xie et al. proposed a quad band metamaterial terahertz absorber which has perforated resonators for ‘0.5-3 THz’ band applications [40]. In another study, a “Cu” -graphene integrated on silicon dioxide glass substrate metamaterial absorber was presented. The main advantage of this design is the tunability characteristics that are controlled by the chemical potential of graphene and the possibility of this absorber in filtering and sensing application [41]. In this perspective, Zhu et al. developed a graphene and vanadium oxide combined metamaterial absorber that has tunable and switchable broadband and multiband property [42]. On the other hand, Isić et al. reported a liquid crystal-based metamaterial absorber for ‘1THz’ center frequency region with tunability characteristics [43]. Moreover, the terahertz metamaterial absorbers can be designed with polarization insensitive and broadband capability by using concentric rings design [44].

Among several available materials, graphene is one of the most widely used materials in terahertz sensing [45] and tunable applications in terahertz bands [46]. On the contrary, it is possible to use non-metallic resonators in a unit cell of designed absorber structure. Cole et al. developed an all-dielectric metamaterial absorber structure without any metallic ground plane for terahertz applications [47]. Most unit cell designs have problems of polarization dependency due to its asymmetric design. To solve this problem, Huang et al. used a symmetric resonator design in each unit cell [48]. Nevertheless, Cheng et al. designed a broadband metamaterial absorber structure which has nearly 270 GHz bandwidth [49]. Meanwhile, black phosphorus and vanadium dioxide combined metamaterial absorber structure were developed by researchers for tunable applications in terahertz range [50]. In the design process of metamaterial unit cell, split ring resonators could be used due to its “LC” resonant characteristics [51,52]. Additionally, there are various approaches reported in literature to design terahertz perfect absorbers [53–56]. For instance, circular ring resonators can be used in many designs for the achievement of polarization independent of metamaterials absorber [57,58].

In this work, a new metamaterial absorber with triple band characteristic is developed numerically and experimentally, which can be applied for imaging in THz range and biological sensing. The proposed structure is composed of three closed circle ring resonators deposited onto the polyethylene terephthalate “PET” substrate, whereas the backside of the design is covered by a metal plate. The novelty of the proposed structure can be emphasized by its simplicity, low profile design and lithographic fabrication onto a flexible substrate of PET. Interestingly, with the collection of these good features, the proposed structure showed a higher Q-factor of 50.72, a larger figure of merit “FOM”, and high sensitivities of the three peaks ‘70.5, 133 and 149.5 GHz /RIU’, which are superior compared to those of the structures reported in literature. The absorption mechanism of the proposed design was comprehensively investigated through the parametric studies and analyses of the “MTM” array unit cell. We also present the electric field and magnetic field distributions. We believe this design can be very useful for the ‘THz’ imaging, filtering, optical communications and sensing applications.

2. Design structure of the MTM unit cell

The metamaterial design structure with a unit cell composed of three closed ring resonators (CRR) that was deposited onto the PET substrate is shown in Fig. 1(a), whereas the backplane of the substrate was completely coated with aluminium metal. Hence, the top-view and section of the unit cell side view MTM structure are respectively shown in Fig. 1(b) and 1(c). The resonators were made of aluminium with a thickness of 0.2 nm and conductivity of 3.56×10^7

S/m, while the dielectric substrate was Polyethylene Terephthalate with a thickness of 10 μm and permittivity of 3.2. The surrounding of the designed structure is air, and the unit cell dimension of the suggested structure was fixed along the “X” and “Y” directions with “ P_x ” 75 μm and “ P_y ” 75 μm , respectively. The other dimensions of the metamaterial design are shown in Table 1. In the design process, it is crucial to consider various parameters including operating frequency range, type of materials, excitation method, and fabrication process. CST Studio Suite based on finite integration technology was used to design, simulate, and optimize the proposed structure. There are several boundary options to be used with the structure for different purposes and applications including periodic, perfect electric conduction, perfect magnetic conduction, open add space, and unit cell. In this work, a unit cell boundary condition was set in the “X” and “Y”- axis while open add space was set in the “Z”-axis, which was used to excite the structure through waveguide ports 1 and 2. This is also compatible with the experimental setup. There are actually significant differences between our work and the work published in [29], in which authors reported a single fixed unit cell of four ring resonators only. However, in our work, we have performed a comprehensive optimization process through variation of the number of ring resonators, their thickness and unit cell size, as well as from the modification of the substrate types and dielectric constants. Therefore, the advantage of the proposed work is to conclude that with the presence of optimized three ring resonators and the employment of flexible PET substrate, it is possible to achieve a triple band-based structure with high absorptivity, and polarization insensitivity, such as, the proposed MTM can be specifically important for the applications of THz images, filtering, biological sensing, and optical communications.

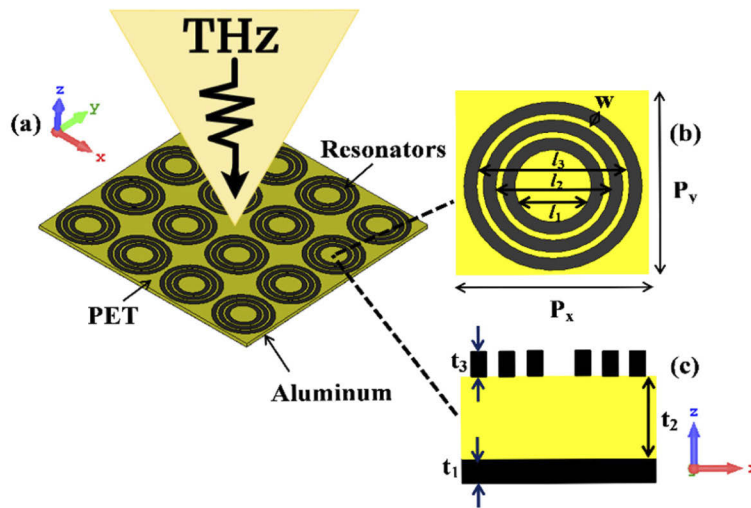


Fig. 1. (a) Perspective view of the three-dimensional proposed structure, (b) top view and (c) sectional side view of the unit cell.

Table 1. Optimal parameters used in this work.

Parameters	Value (μm)	Parameters	Value (μm)
P_x	75	l_3	60
P_y	75	t_1	0.2
W	10	t_2	10
l_1	30	t_3	0.2
l_2	45		

Figure 2(a) shows the simulated reflection, absorption, and transmission spectra of the proposed metamaterial absorber over the frequency range of ‘0.2-1THz’. The reflection coefficient of the proposed structure has three resonance frequencies at 0.43, 0.61, and 0.88 THz with magnitudes of 0.1, 0.3, and 0.1, respectively. Correspondingly, based on the simulation results, the absorption spectra are integrated around the PET layers. When the substrate layer is incorporated with three ring resonators, the characteristic absorption peaks are merged together to expand the absorption bandwidth, thereby showing three highly resonance peaks. The absorption spectrum showed three intensive peaks at the same resonance frequencies of ‘0.43, 0.61, and 0.88 THz’ with the absorptivity of 98%, 91%, and 98%, respectively. The transmission value is almost zero over the frequency range of interest due to the backed ground plate of the structure. Figure 2(b) shows the equivalent circuit diagram of the unit cell structure of the ‘MTM’ resonator. The innermost closed ring can be represented by a parallel ‘LCR’ circuit because of its relatively smaller radius compared to those of the second and the third (outermost) closed rings, so there would be a high probability of stronger electrical coupling between the upper and lower arms of the innermost ring. On the other hand, the middle and the outermost rings can be represented by a series ‘LCR’ tank. Moreover, the electrical capacitive coupling between the innermost and the middle ring as well as between the middle and the outermost ring can be represented by the capacitors ‘C4’ and ‘C5’, respectively. However, due to the symmetry nature of the ‘CRR’, it is possible to divide the ‘C4’ and ‘C5’ capacitances. Therefore, in Fig. 2(b) the passive ‘R’ and ‘L’ elements with subscripts from 1 to 3 are assigned to the innermost, middle, and outermost CRR, respectively.

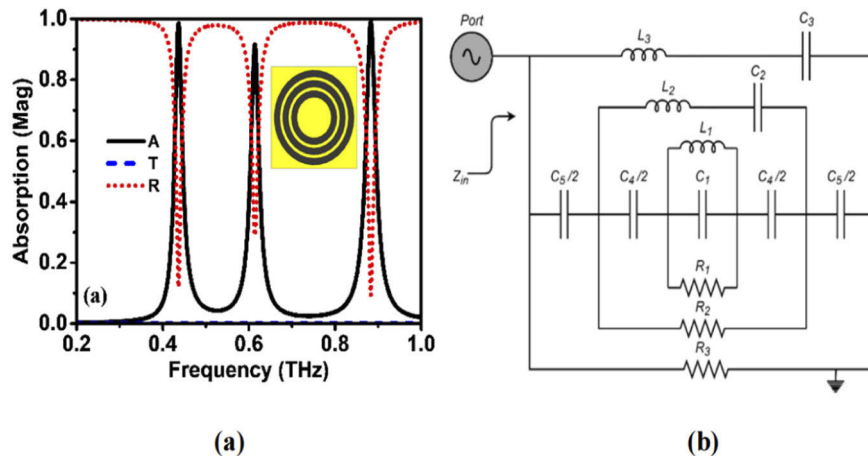


Fig. 2. (a) Simulated reflection, absorption, and transmission spectra of the proposed design and (b) its equivalent circuit diagram.

3. Design procedure of the proposed metamaterial unit cell

With the aim of achieving optimum yields and further understanding of the working mechanism, various designs of the metamaterial structure were analysed, as shown in Fig. 3. Each of the designed structure was simulated over the frequency range of ‘0.2-1 THz’. The reflection and absorption coefficient results are illustrated in Fig. 4. Starting with a single Closed Circular Ring Resonators CCRR, as represent in design 1, design 2, and design 3, having different resonator radii, the structures are operated at different frequencies. The ‘CCRR’ in design 1, with the smallest radius, provides the highest resonance frequency around ‘0.88 THz’ with a reflection coefficient value of 0.38. Design 2 has a greater resonator radius, which provides a resonance frequency around ‘0.6 THz’. In design 3, the larger the resonator radius possesses the lower

resonance frequency around ‘0.41 THz’. It is important to mention that design 1 has a lower absorption value among these three designs, while design 3 has the best absorption with almost perfect absorption. The dual “CCRR”, in a single structure was also investigated, as represented in design 4, design 5, and design 6. These designs provided a dual resonance frequency due to the presence of dual resonators. Design 4, which is comprised of design 1 and design 2, showed two distinct resonance frequencies of ‘0.88 and 0.6 THz’. Due to the coupling effect between the small and medium resonators in design 4, the absorption value was improved and reduced to ‘0.41 THz’. The best absorption performance was achieved at the frequencies ‘0.4 and 7.8 THz’ by using both the smallest and the largest resonators together in design 5. Similarly, design 6 has led to produce resonance frequencies at ‘0.41 and 0.6 THz’. Hence, based on the studied designs, a three CCRR incorporated design was proposed with different radii for the “CCRR”. The proposed absorber has three highly absorption peaks at ‘0.43, 0.61, and 0.88 THz’ with absorption values of 99%, 92%, and 99%, respectively. To obtain the desired performance of the resonator, it is crucial to study the effect of the width of the resonators and the size of the gaps between resonators on the absorption peaks.

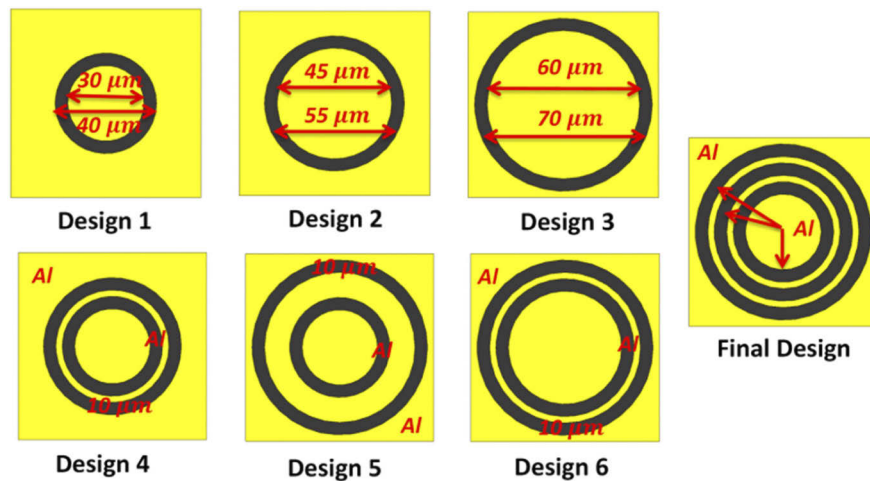


Fig. 3. Different design layouts were analyzed for selecting the final design.

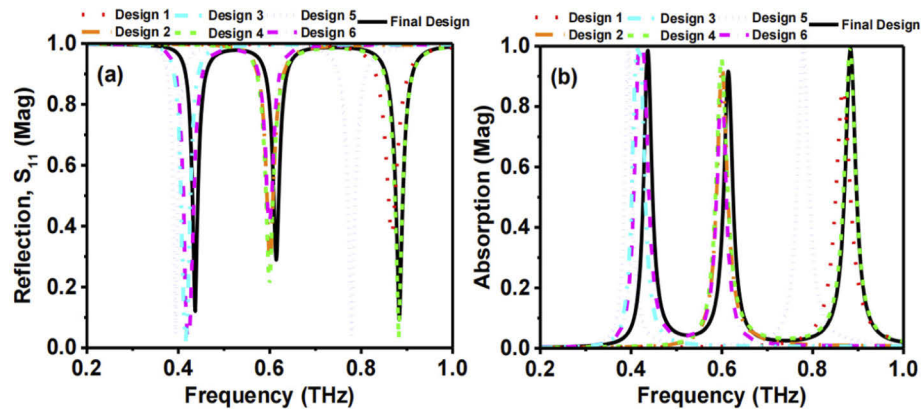


Fig. 4. (a) Reflection (S_{11}) and (b) absorption spectra for different layouts of the resonators.

4. Simulation results and discussion

4.1. Effect of the variation of the dielectric constant of the substrate and different types of substrate material

To show the effect of substrate dielectric constant (ϵ) on the reflection coefficient, all other parameters were kept fixed, while the substrate dielectric constant was changed from 2.8 to 3.6 with a step of 0.2. The obtained reflection coefficients from '0.01 to 1 THz' are shown in Fig. 5. Since the reflection coefficient can be explained in terms of the resonance frequency (ω) and that the capacitance of the substrate is directly proportional to the dielectric constant ($C = \epsilon A/d$), any increase in the dielectric constant has led to decrease the resonance frequencies, as shown in Fig. 5(a) and 5(b), where the resonance frequency decreases from '0.45 to 0.4 THz' in one hand. On the other hand, the increase of dielectric constant led to shift back of the resonance frequency expectedly. This simulation is important to show the proposed structure's operation principle and linearity, which are important parameters in the metamaterial studies. Furthermore, the best absorption values obtained with the proposed substrate are shown in Fig. 5(b).

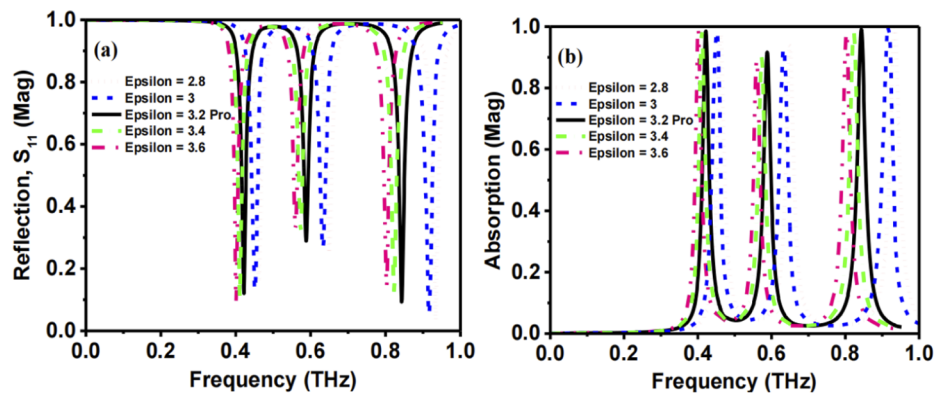


Fig. 5. (a) Reflection (S_{11}) and (b) absorption spectra of the proposed design with different dielectric constants of the proposed resonator.

The proposed design was investigated under four different substrates. There are several materials reported in the literature and found in the market such as FR4 and Rogers. They are mostly used as a substrate layer in various applications. In this study, we have tested FR4 and Rogers materials for dielectric variations and their effects. In some printed circuit board "PCB" process, FR4 and Rogers 5870 are difficult to apply to the terahertz frequency band. We have used the PET dielectric layer as a substrate due to its ease of implementation in the lithographic technique for the terahertz frequency regions. The obtained reflection versus frequency plot is presented in Fig. 6(a). As explained before, the dielectric constant is inversely proportional to the capacitance. The increase in capacitance leads to the decrease in the resonance frequency and vice versa. Additionally, we have to take into account the loss in material substrate and its effects on the reflection coefficient. The complex dielectric constant can be expressed as ($\epsilon = \epsilon' - j\epsilon''$). The complex dielectric function or relative permittivity is a materials property depending on frequency, temperature, pressure, and structure. According to the statistical mechanics, both " ϵ' " and " ϵ'' " have direct physical interpretation. The real part, " ϵ' ", is an indication of the degree to which a material can be polarized and it is a component quantifying the stored energy (the real part is directly proportional to the field amplitude, while the imaginary part " ϵ'' " is associated with the dielectric losses defining the energy dissipated per cycle. In technical application of dielectric relaxation spectroscopy, the dissipation factor ($\tan\delta = \epsilon''/\epsilon'$) is important in the

materials characterization “ f ” [59]. A backshift in the resonance frequency and the effects of loss tangent as a result of the increase of dielectric constant were clearly seen in Fig. 6(a) and 6(b).

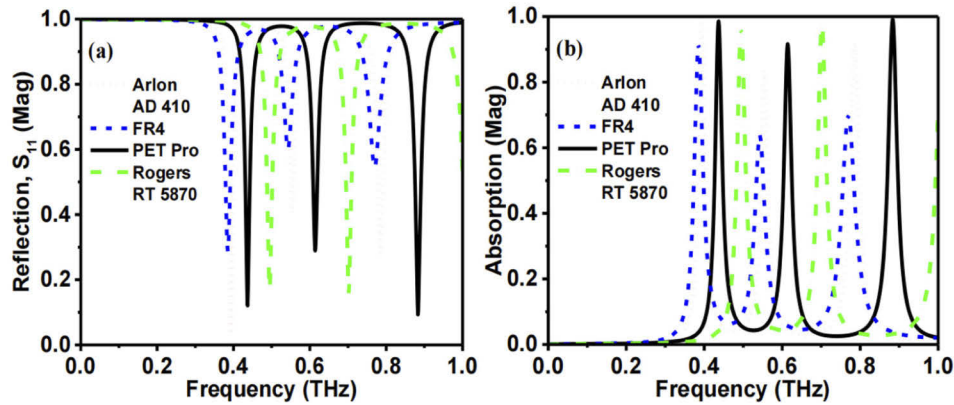


Fig. 6. (a) Reflection (S_{11}) and (b) absorption spectra of the proposed design under different types of the resonator's substrate.

4.2. Effect of the different widths (w) of the resonators

Figure 7(a) and 7(b) show the simulated results of the effect of the width of the resonators on the reflection coefficient when the width of resonators is increased. It can be found that the resonance frequency has shifted back (red shifted) for all three resonance frequencies. According to the “LC” circuit model, the resonance frequency is inversely proportional with the width of the resonators, i.e., $(f_r = 1/2\pi\sqrt{LC} = C_0/\pi W_q\sqrt{\epsilon_r})$, such that the “LC” – circuit concept is still valid for the involved resonant behaviour. Upon looking into Fig. 7(a), one can observe that the resonance frequency has shifted from ‘0.44 to 0.39 THz’ by changing the width of the resonator from 6 to 14 μm at first resonance point. This explanation is valid for the other three resonance peaks, which are resulted by the three resonators. Almost ‘1 THz’ tuning option is available at the third resonance points when the width is changes by 8 μm .

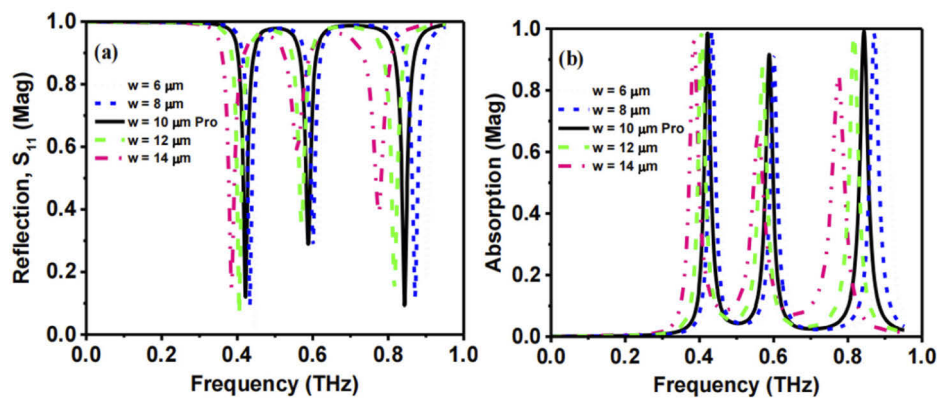


Fig. 7. (a) Reflection (S_{11}) and (b) absorption spectra of the proposed design for different widths of the resonator.

4.3. Effect of different thicknesses (t_2) of the substrate

In this part of the study, the thickness of the intermediate FR4 layer was modified by keeping all other parameters constant. The obtained reflection coefficient was plotted in Fig. 8(a) and 8(b). It was seen that the resonance points are shifted back when the substrate thickness was reduced from 16 to 10 μm . However, the less resonance frequency shift was observed at the first resonance point, which was around '0.4 THz'. An interesting condition was found for the substrate's thickness in which the "LC" resonance is invariant below 14 μm . This is resulted due to the effect of the material's dielectric constant since ($n_{\text{eff}} = C_{\text{sub}}n_{\text{sib}} + C_{\text{air}}n_{\text{air}}$), which are coefficients for the substrate and air contributions, respectively [60]. Since the "FR4" dielectric constant is high, we expect to see a trivial effect on the reflection coefficient, as was verified from the simulated results.

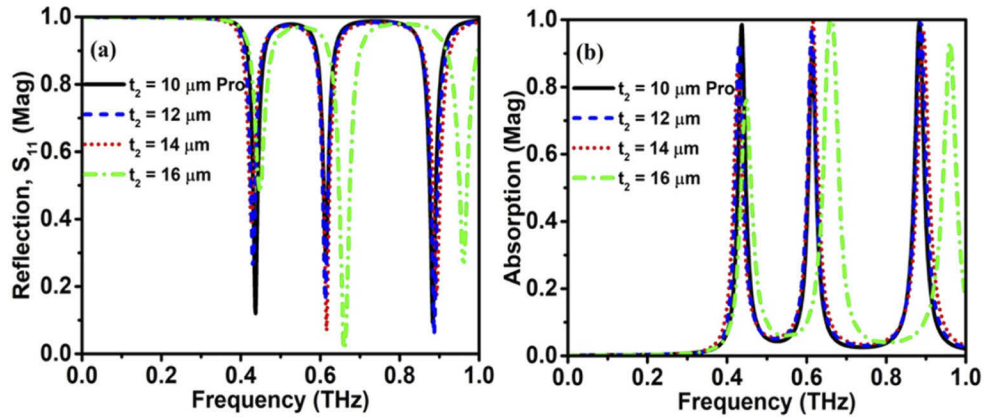


Fig. 8. (a) Reflection (S_{11}) and (b) absorption spectra of the proposed design under different thicknesses of the substrate.

4.4. Analysis of the axis of the waveguide port

In the simulation software, we have used the electric ($E_t = 0$) and magnetic ($H_t = 0$) boundary conditions to the "X" and "Y" axis, respectively, while the open add space was applied to the "Z"-direction. In this section, we simulated the waveguide port position and obtained the resulting S-Parameters by applying the waveguide port in the "X"- and "Y"-axis directions in contrast to the "Z"-axis, to show which position can provide a better result.

Since the applied electromagnetic field must induce magnetic field to create resonance frequency by the resonators, minimum effects were seen by the flux application in the "X"- and "Y" axis, as shown in Fig. 9(b) and 10(b). This can be theoretically understood from ($r(f) = \sqrt{R(f)}$), revealing the field reflection coefficient as a function of frequency calculated from the reflectance spectrum, and θ is the phase change introduced by the structure. Refractive index, ($\tilde{n} = n + ik$) of the sample can be then determined at each wavelength when reflectivity "r" (w) is measured, while the phase " $\theta(f)$ " is derived via Kramers-Kronig relation from "r(f)". It is usually possible to calculate the reflectivity and phase changes from a single reflection for the entire number of "N" reflections [61,62]. Due to the phase angle " θ " reflection coefficient, the induced electric and magnetic fields become smaller between front and back sides of the resonator, which result in unwanted reflection and transmission coefficients.

$$\begin{aligned} n &= 1 - r^2 / (1 + r^2 + 2r \cos \theta) x n_1 \\ k &= -2r \sin \theta / (1 + r^2 + 2r \cos \theta) x n_1 \end{aligned} \quad (1)$$

After the results were obtained for the S-parameters, it was concluded that the wave propagations did not exhibit the appropriate resonance frequencies. In the meantime, by simulating the wave propagation in the “Z”-axis, a superior result was obtained for the reflection coefficient. Hence, as a result of the lack of resonance frequencies and distinct properties, “X” and “Y” -axes wave propagations were rejected.

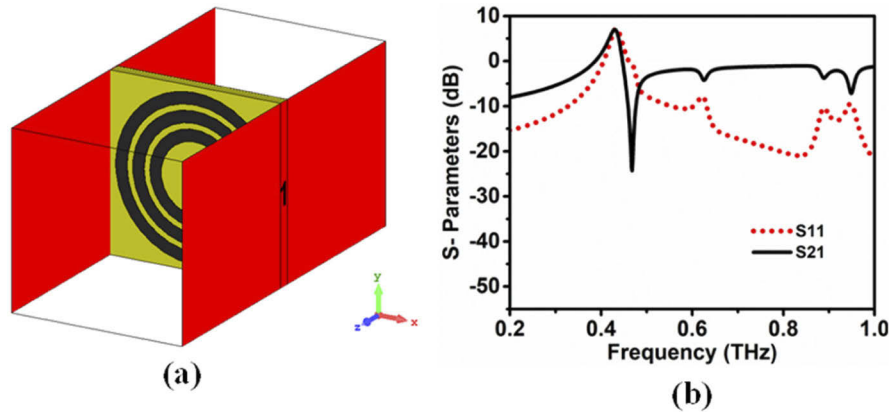


Fig. 9. (a) Simulated experimental set up showing x-axis waveguide ports and (b) S-parameters for the recommended unit cell.

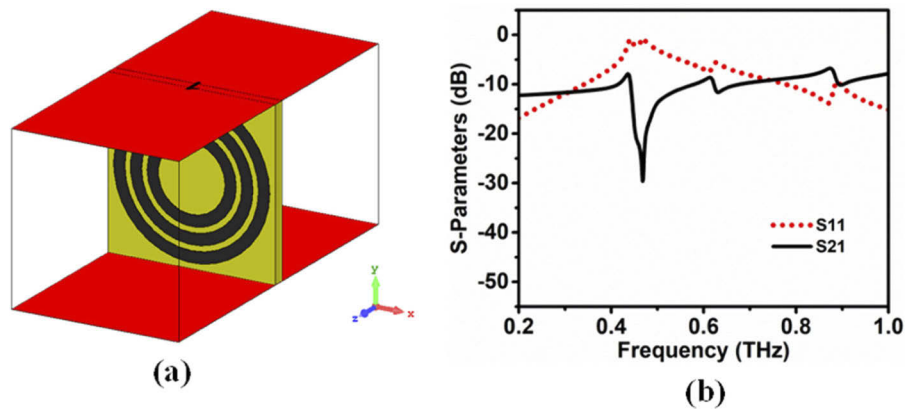


Fig. 10. (a) Simulated experimental set up showing y-axis waveguide ports and (b) S-parameters.

4.5. Effect of dimension (D) variations of the unit cell

Finally, we have simulated the substrate dimension to show its effects on the resonance frequency by realizing five different set of simulations. This is where the plasma frequency can be calculated using the quasi-static approximation [63,64]:

$$k_p = 1/D \sqrt{\frac{1}{2\pi} \ln \frac{D^2}{4r_0(D-r_0)}} \quad (2)$$

where r_0 is the radius of the metallic vias. Since frequency is inversely proportional to the slab length D , it is decreased with the increase of D , as shown in Fig. 11. To verify this, we did

simulation for five different lengths of the substrate, to be changed from “65×65 mm²” to “85 × 85 mm²” with a step of 5. Due to mutual effects of electric and magnetic fields, the resonance level is not changed. Furthermore, the attractive resonance frequency shift is remarked when the dimension is set from 65 to 70 mm².

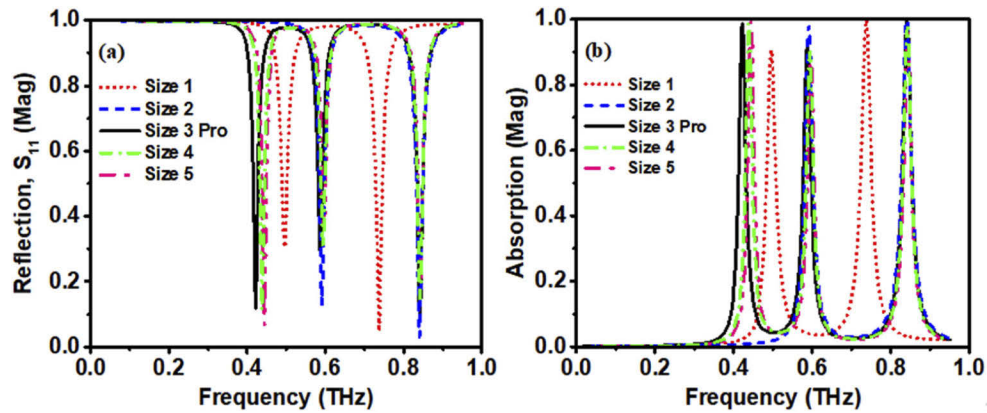


Fig. 11. (a) Reflection (S_{11}) and (b) absorption spectra of the proposed design under variation of the unit cell.

4.6. Analysis of the MTM array of the unit cell

In this section, the proposed multi-band metamaterial absorber was analysed based on the utilization of different unit cell formations. Generally, different formations and arrangements of absorbers are required for different applications. For instance, in a large antenna array, the 1×2 array is widely used as a decoupling structure between antenna elements. On the other hand, enormous numbers of unit cell formations are employed in military radar applications to cover large areas. As a result, it's critical to investigate different absorber arrangements that can be used in a variety of applications.

In the simulation program, we have used the electric ($E_t = 0$) and magnetic ($H_t = 0$) boundary conditions for both, “X” and “Y” - axis, respectively, while the open add space was applied for the “Z”- direction. In general, a single unit cell of MTM cannot function on its own, it requires an array of unit cells to demonstrate acceptable exotic EM properties. On the other hand, a MTM containing electrically conductive parts is referred to as an array, which has sufficient capacitive and inductive properties. Figure 12 shows all the investigated arrangements of the proposed “MTM” absorber including unit cells of 1×2 array, 2×2 array, 3×3 array, 4×4 array and fabricated image. For achieving accurate results, the same environment and condition were set for the proposed structure in the rest of the arrangements. Each arrangement was simulated individually, and the reflection coefficient results and absorption responses were compared, as shown in Fig. 13. All four array cells delivered triple resonance frequencies in the THz-band. The magnitude values and frequency deviated slightly from the unit cell results. Overall, the findings showed that the resonance frequencies have shifted in response to the higher or lower frequencies, which were dependent on the number of array elements. In other words, rather than being impacted parallel to the array metamaterial, the propagation constant was influenced orthogonally.

It can be observed from Fig. 13 that relatively the same results were achieved from all the arrangements, in which they provided three absorptions pecks over the frequency range of interest. However, there are frequency shifts from different arrangements. The results of the 2×1 , 2×2 , and 3×3 array are quite similar to each other, where the three structures have small reflection

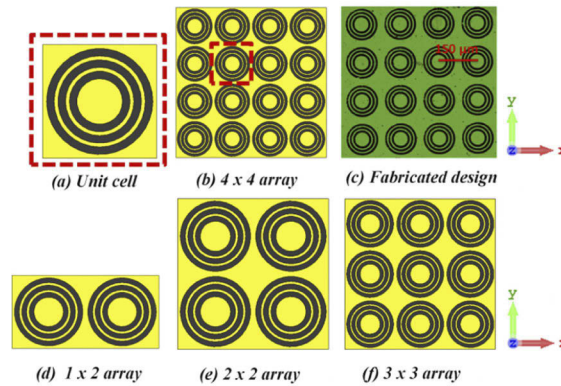


Fig. 12. (a) Simulated arrangement of unit cell structure (b) simulated arrangement of 4×4 array of the proposed structure, (c) image of the fabricated design and (d) to (f) are the unit cell of 1×2 , 2×2 , and 3×3 array, respectively.

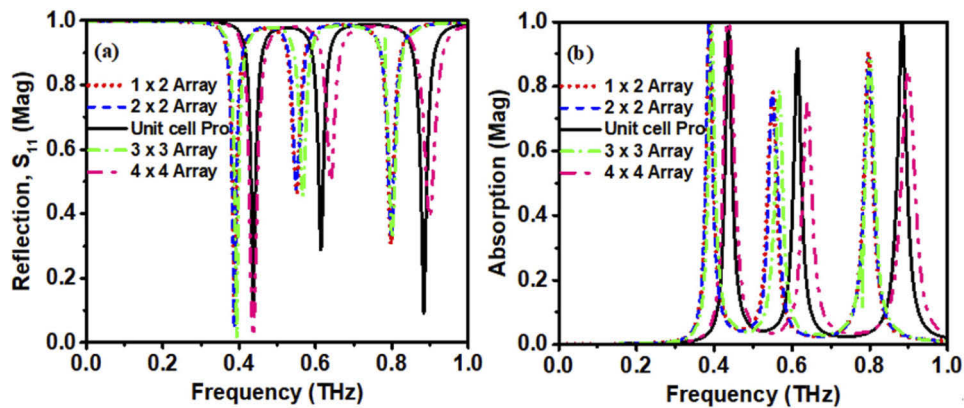


Fig. 13. (a) Reflection (S_{11}) and (b) absorption spectra of the proposed design under different arrays of the closed ring resonators “CRR”.

values of around 0.2, 0.5, and 0.3 at frequencies of ‘0.39, 0.56, and 0.79 THz’. It is also worth mentioning that the absorption of these three structures has lower values by about 10% at the second and third resonance frequencies compared with the proposed design. The results of the 4×4 array indicated that the absorption peaks were occurred at relatively similar frequencies of ‘0.43, 0.61, and 0.88 THz’ with a slight shift of the second and third frequencies towards higher frequencies. The absorption ratio of the 4×4 array was also reduced at the second and third absorption peaks by about 10% compared to that of the proposed unit cell structure.

4.7. Polarization independent

To study the effect of incidence angle variation on the absorption characteristics, the incidence angle “ θ ” for both transvers electric “TE” and transvers magnetic “TM” was changed from 0° to 90° in seven steps and the other parameters remained constant during the simulation process. As it can be seen from Fig. 14(a) and (b), when the polarization angle is changed, the absorption of the proposed structure remains the same and counted to be more than 90% at the resonance frequencies. This indicates that the proposed absorber is insensitive to the incidence angle of the incoming wave for both TE and TM modes. The sensitivity of the proposed metamaterial

absorber to the polarization of the incident wave was numerically investigated and the obtained results are shown in Fig. 14(c) and (d) for both “TE” “TM”. For this purpose, the direction of the propagating EM wave was fixed at normal incidence, while the direction of “E”-Field and “H”-field were changed at different polarization angles “ φ ” from 0° to 90° with a step size of 15° . As it is clearly seen from Fig. 14(c), the absorption curve remained almost the same with the change of polarization angle over the entire frequency range. Figure 14(d) shows the effect of variation of polarization angle on the absorption spectrum. One can see from the curve that the absorption remains constant in the frequency range from ‘0 THz’ to ‘1 THz’. Therefore, it is concluded that the proposed “MTM” absorber is independent on the polarization of electromagnetic waves. These two features of the proposed “MTM” absorber (insensitive to polarization and incident angle) can be considered as one of the most important properties of the proposed absorber, which are highly required for some specific applications.

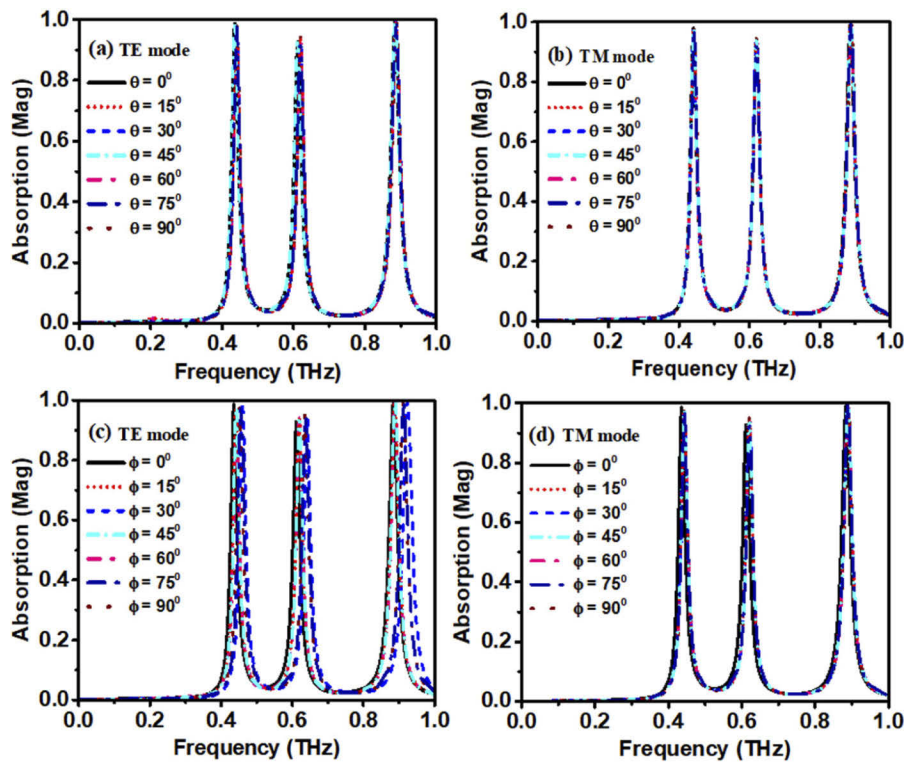


Fig. 14. (a) Simulated absorption spectrum at different incident angles for TE mode (b) TM mode, (c) The polarization independent of the final design from 0° to 90° for “TE” and (d) “TM” modes.

5. Experimental results and discussion

In this work, proposed design was fabricated according to the following steps, as shown in Fig. 15(a), a 13 μm -thick “PET” layer with 200 nm coated aluminum film was utilized. Initially, a 3 mm quartz wafer was cleaned by ethanol and acetone. Later, the cleaned “PET” -aluminum film was placed carefully onto the surface of the wafer using tweezers. After a while, acetone was volatilized and hence it was necessary to press the two layers quickly and precisely in order to minimize the air between the material and the wafer surface. Due to the relatively flat surface, the material seemed to be adsorbed to the wafer. Then, positive liquid photoresist RZJ-304 was

spin-coated onto the sample, and then baked for 90 s in an oven at 100 °C. Finally, the sample has been transferred to the photolithography processing system and set out to fabricate “60×60 mm²” array on the sample. When it was processed, the part of altered photoresist properties was cleaned with developer for 30s. Then, the aluminum etching solution was used to etch the exposed metal. By this, we would get the metamaterial structures. At the end, the sample was cleaned by acetone to remove the rest of the photoresist. Finally a 200 nm-thick metallic Al layer was deposited on the other side of the “PET” layer through vacuum evaporation technique. As such, a metamaterial of “60×60 mm²” periodic metallic arrays with the size of “9×9 mm²” was fabricated, an optical microscopy image of a portion of the fabricated absorber structure is shown in Fig. 15(b). The reflection spectra were characterized using terahertz time-domain spectroscopy. The studied sample was illuminated by a light source with the spot diameter of 6 mm, and the periodic boundary condition was considered.

Figure 16 shows the comparison of the reflectivity and absorptivity between the simulated and experimental results in the frequency range of ‘0.2 to 1 THz’. One can see from the simulation results that there are three absorption peaks at ‘0.51, 0.68, and 0.98 THz’, which correspond to the absorptivity of 98%, 91%, and 98%, respectively. Comparably, the experimental results showed three peaks at ‘0.43, 0.61, and 0.88 THz’, corresponding to absorptivity of 82%, 79% and 84%, respectively. It is worth to point out that a trivial variation was observed between the numerical and experimental results, especially around the third resonance peak, which is yet within a reasonable range in agreement with the simulation results, which may be attributed to the presence of impurities and un corroded aluminum during the fabrication. In the lithography processing, when the chip is immersed into the aluminum etching solution, one can only control the time to make the three closed rings as perfect as possible. But the result is influenced directly by the existence of imperfections and perhaps the metal had been relatively oxidated before test. The size and thickness of the chip are also slightly different from the simulation. In addition, due to the high flexibility of the PET substrate (with thickness of $\approx 13 \mu\text{m}$), there have been some undesired deformations in the fabricated samples, and the surface flatness of the structure can have some effects on the absorption. Also, because of the existing experimental conditions, the spectral quality is not ideal. Hence, our future attempt can be made to improve the signal-to-noise ratio of the measurement system in the aspects of increasing the signal collection time and restraining noise to improve the spectral quality.

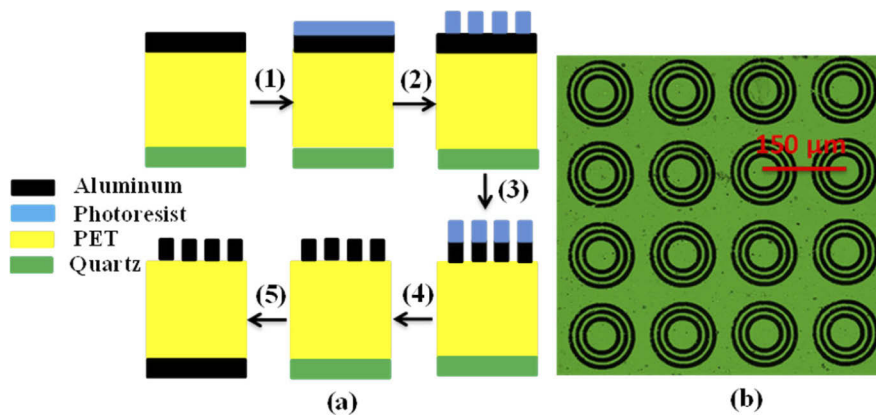


Fig. 15. (a) Process flow: (1), (2) photolithography to define the metamaterial geometry, (3), (4) wet etching and washing of the photoresist to fabricate the metamaterial structures, (5) evaporation of metallic substrate layer on other side of “PET” layer; (b) optical microscopy image of fabricated absorber structure.

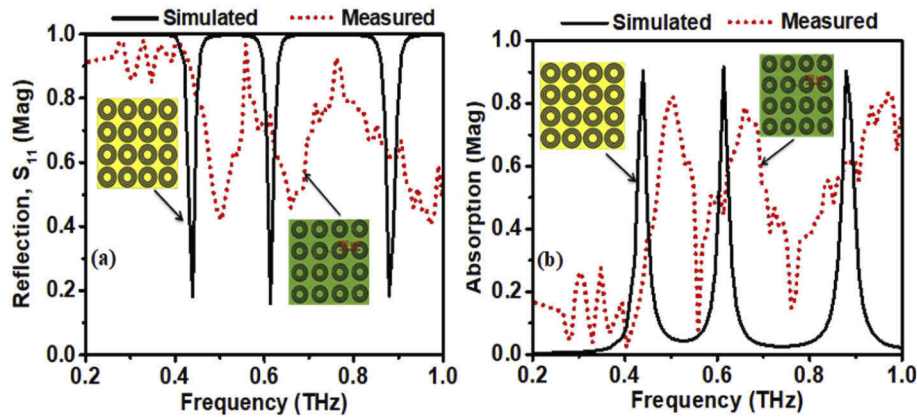


Fig. 16. Comparison between the simulated and experimental results for the (a) reflection (S_{11}) and (b) absorption spectra.

5.1. Electric field and magnetic field analysis

Consequently, the electric field strength was observed to be stronger at the right side of the “CRR” compared to that accumulated at the left side, as shown in Fig. 17. However, at the low resonance frequency of ‘0.43 THz’, the electric field strength on the left arc of the outermost ring was found to be stronger compared to that appeared on its right arc. The same trend was seen to be true for the middle and innermost rings at the higher resonance frequency of ‘0.61 and 0.88 THz’, respectively. The consequence of this non-uniformly distributed electric field strength across the “CRR” can be ascribed to the different capacitive electrical couplings that are generated between the three closed rings. Literally, the capacitive coupling is going to be originated due to the current movement from the right side to the left side of the “CRR”. As such, the intense electric field along the left arcs of the rings suggests that the current flow is getting increased to the left arc of the outermost ring, middle ring, and innermost ring sequentially when the resonance frequency is increased.

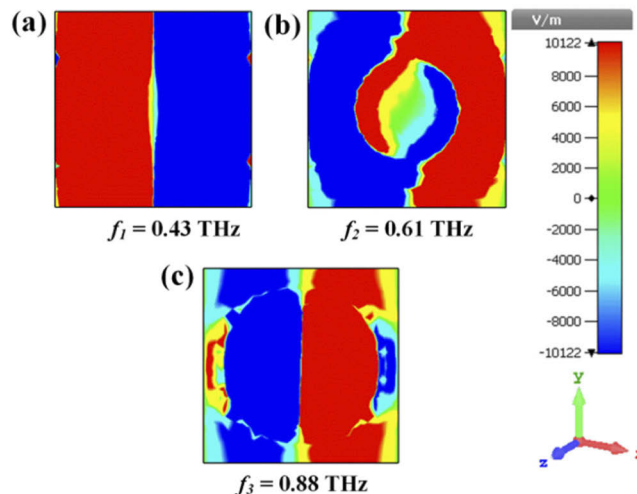


Fig. 17. Simulated electric field distribution at three different resonance frequencies (a) ‘f’ ‘0.43 THz’, (b) ‘0.62 THz’ and (c) ‘0.88 THz’.

Figure 18 shows the magnetic field strength induced across the proposed “CRR” structure at the three defined resonance frequencies. The magnetic field strength is directly influenced by the induced magnetic field due to the circular movement of the current flow. For instance, in the places where the current loops are parallel, the induced magnetic fields act upon enhancing the overall magnetic flux. On the contrary, the net magnetic field that is induced by the antiparallel currents is going to be neutralized. One can see that the magnetic field strength across the “CRR” is generally weak, which can be attributed to the presence of counterclockwise and clockwise flow of electrons in the rings, thereby neutralizing the induced magnetic field. Nevertheless, the magnetic field strength is relatively strong at the boarder of the outermost and innermost rings due to the unidirectional flow of currents. Supportably, at the high resonance frequency of ‘0.88 THz’, the magnetic field strength has become stronger at the center of the innermost ring compared to those at the other resonance frequencies.

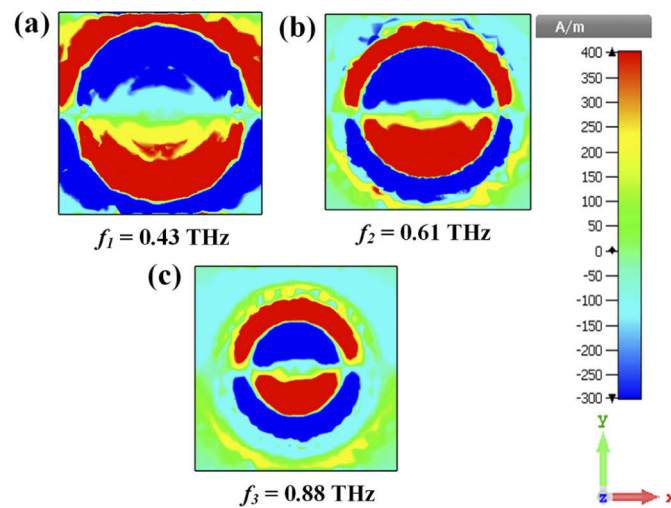


Fig. 18. Simulated magnetic field distribution at three different resonance frequencies (a) ‘ f_1 ’ ‘0.43 THz’, (b) ‘ f_2 ’ ‘0.62 THz’ and (c) ‘ f_3 ’ ‘0.88 THz’,

5.2. Refractive Index sensing performance

In this section, we investigated the sensing performance of the proposed triple band “MTM” structure by changing the refractive index (n) of the surrounding and the results is illustrated in Fig. 19. For obtaining the sensing effect, we must increase or broaden the sensing place to achieve the accurate absorption effect. Figure 19(a) displays the effect of the variation of the refractive index of the surrounding on the absorption spectrum. In the simulation software, we examined the absorption spectra dependence on the refractive index with overall layer’s thickness of 20.4 μm . When the refractive index was changed from 1 to 1.8 in steps of 0.2, while other dimensions were kept constant,, all the three resonance frequency peaks were red shifted from the left to the right side. . In the present paper, the sensitivity of the proposed design can be denoted by S and defined as $\Delta f/\Delta n$, where Δf and Δn are the change of the value of the frequency peak and refractive index of the surrounding respectively [54]. Figure 19(b-d) shows the comparison of the peak frequency and fitting results for the three frequency peaks, The peak frequency is inversely proportional to the refractive index and the sensitivity of the three peaks can be found from the slope, which corresponding to the extracted refractive index of ‘70.5, 133, and 149.5 GHz /RIU’ from the linear fitting, respectively.

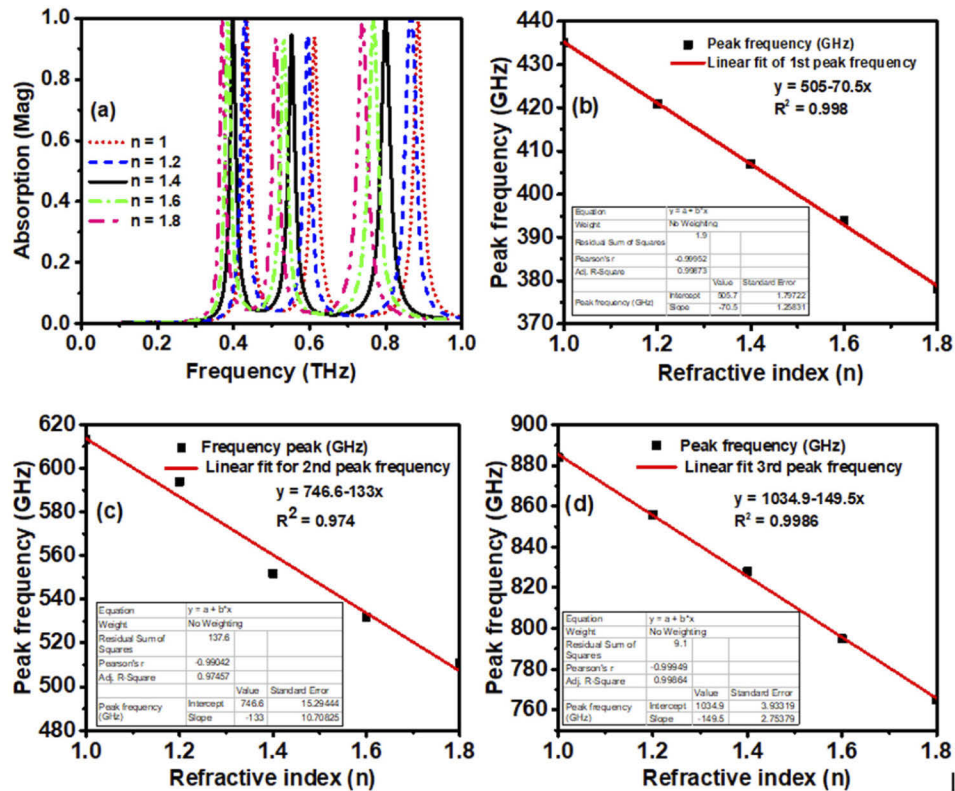


Fig. 19. (a) Absorption spectrum dependence on variation of refractive index for the surrounding, and (b–d) shows the resonance frequency peak with linear fit of the three frequencies versus refractive index.

In this section, we investigated the effect of variation of the analyte depth on the absorption of the proposed structure. In the simulation software, we have set the analyte thickness to 10 μm . As shown in the black curve of Fig. 20 (a), for the first resonance peak the absorption is about 99.17% at 0.37 THz. By increasing the analyte depth, the resonance frequency shifted to a lower frequency, but the absorption peaks remained stable. The absorption of the second and third resonance frequencies were 93.77 and 99.03% which correspond to the frequency of 0.52 and 0.76 THz, respectively. When the thickness of the analyte was increased from 10 to 40 μm , the resonance frequency was shifted to the lower frequency. The absorption spectrum for the second peak is higher, which is equal to 99.98% at 0.51 THz, but for the third peak, the absorption has been lower at 40 μm depth, which was around 78.75% at 0.75 THz. This is where at 5 μm the absorption showed the largest value of 99.99% at 0.78 THz (Blue curve). In addition, we specifically examined the resonance frequency shift of the three peaks in the case of intrinsic resonance (i.e., without any coated layer) for different thicknesses of the analyte layer, as shown in Fig. 20(b–d). When the thickness of the analyte was changed the corresponding shift in the resonance frequency was observed for each peak. It was concluded that the increase in the analyte depth has led to decrease the resonance shift. However, at around 10 μm , it attained almost a constant value.

Figure of merit “FOM” is another important parameter used to compare the sensing performance of various sensors, which is define as the ratio of sensitivity to the full width at half maxima

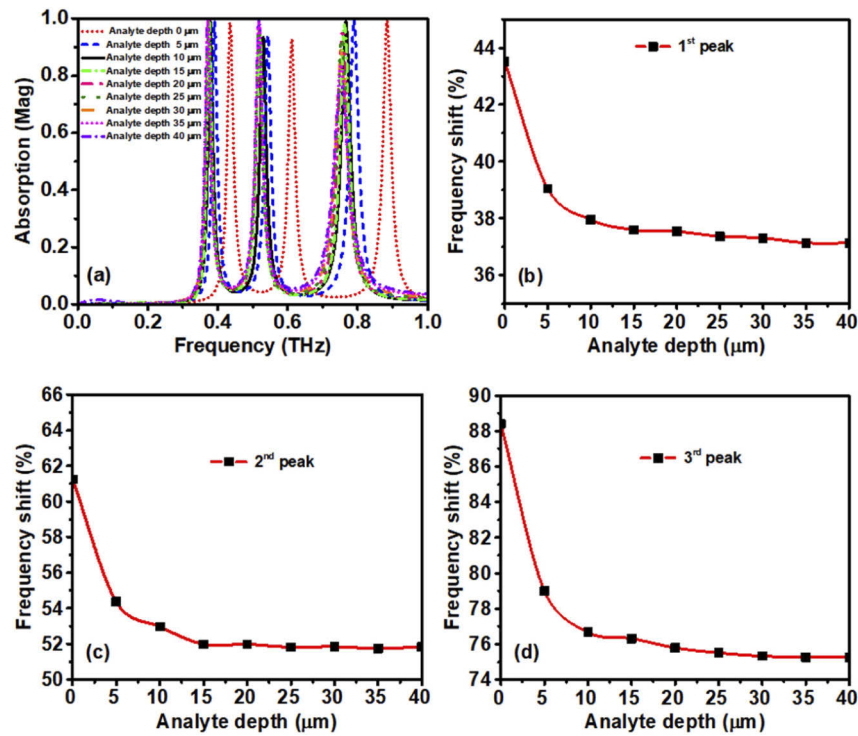


Fig. 20. (a) Absorption spectrum dependence on variation of analyte depth and (b–d) shows the frequency shift versus different analyte depth.

“FWHM” [65]:

$$FOM = \frac{S}{FWHM} \tag{3}$$

We analyzed the figure of merit “FOM” of the three resonance peaks with varied thickness of the analyte layer, as shown in Fig. 21. In the proposed design, the FOM was found to be 3.17, 6.29, and 5.69 for the 1st, 2nd and 3rd peak, respectively. The suggested refractive index sensor design has a high sensitivity towards sensing biological samples. Additionally, its high FOM makes it an excellent biological sensor.

Table 2 shows the sensitivity of the proposed structure to the refractive index (n) and figure of merit (FOM) in comparison with other published results in literature [54,56,66]. The sensitivity and FOM for the suggested design were found to be higher compared to those of other designs reported before. The results obtained in this work confirm the viability of our design for the sensing applications [12,54].

Table 2. Sensitivity comparison for the proposed MTM sensor with other similar works.

Ref.	Frequency band (THz)	S(GHz/RIU)/Peak 1	S(GHz/RIU)/Peak 2	S(GHz/RIU)/Peak 3	(FOM)
54	0.15-0.85	54.18	119.2	139.2	0.52, 1.19, 3
56	0.1-1	72	103.5	139.5	3.6, 5.17, 5.81
66	0.2-1.16	52	119	149	0.12, 0.38, 0.4
This work	0-1	70.5	133	149.5	3.17, 6.29, 5.69

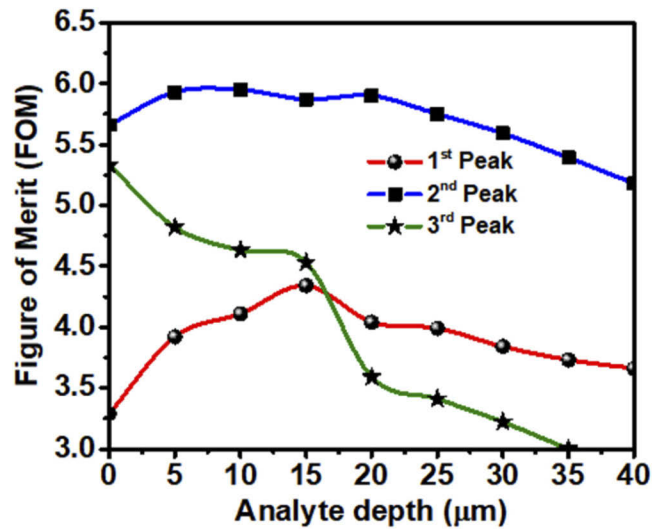


Fig. 21. Figure of Merit (FOM) spectrum dependence on variation of analyte depth corresponding to three different resonances.

Table 3 shows the obtained results of the proposed design compared with other reported metamaterials THz absorber in terms of resonator shape, waveband, overall unit cell size, substrate materials, absorptivity, peak numbers and fabricated structure. The proposed design was fabricated and tested using lithography techniques which are very important in THz devices. Results showed that the proposed structure outperformed those reported in literature.

Table 3. Comparison between the proposed and existing tri-band metamaterials in terms of various features.

Reference	Shape of the MTM Unit Cell	Frequency operating THz	Unit cell size (μm^2)	Absorptivity	Peak Numbers	Experiment (practical)
[28]	Windmill square ring	0-4	70×70	99.43, 99.92, 99.5	3	No
[53]	rectangular strip resonator	0.8-3.7	60×60	99.98, 99.99, 99.98	3	No
[56]	Three quadratic resonators	0.1 - 1	75×75	99.5, 86.4, 98.4	3	yes
[54]	array of planar metallic resonators	0.15-0.85	300×300	80, 81, 79	3	Yes
[55]	Jerusalem cross array resonator	0.1-1	200×200	97.6, 96.5, 84.1	3	No
[48]	Complementary ring resonator	1 - 6	30×30	99.4, 99.6, 98.2	3	No
current work	Closed Circle ring resonators	0 - 1	75×75	98, 91, 98	3	Yes

Table 4 shows further comparison of the proposed design with the other “MTM” absorbers. The comparison has been done according to the materials structure layer, bandwidth, Q-factor polarization angle and publication year. As can be seen in Table 4, the recommended design characterized by a very high Q-factor and insensitive polarization angle from 0° to 90°.

Table 4. Comparison between the proposed structure and existing MTM absorber.

Ref.	Techniques used	Materials substrate	Q-factor	Polarization	Angles (degree)	Year published
[28]	Gold resonators / polyimide / buck Dirac semimetals	polyimide	13.5	Insensitive	TE and TM	2019
[53]	Au resonators/ dielectric/Au	dielectric slab	37.50	Sensitive	—	2019
[56]	Al resonators / PET/ Al	PET	11	Insensitive	0 - 70	2021
[54]	Al resonators / polyimide /Al	polyimide	5.5	sensitive	—	2015
[55]	Au resonators / Si / Au	Silicon	26	Insensitive	0 - 45	2015
[48]	Au resonators / GaAs / Au	GaAs	19.78	Insensitive	0 - 45	2018
This Work	Al resonator /PET/Al	PET	50.72	Insensitive	0 - 90	2021

6. Conclusions

A ‘THz’ operated “MTM” perfect absorber was successfully developed and investigated numerically and experimentally. The proposed design consists of three closed circle ring resonators loaded onto the “PET” substrate and backed by Al to illuminate electromagnetic waves. The proposed absorber showed three absorptivity peaks of 98%, 91%, and 98% at the resonance frequencies of ‘0.43, 0.61, and 0.88 THz’, respectively. The recommended “MTM” triple design was characterized by its higher sensitivity compared to those reported in literature. The sensitivity of the three peaks to the surrounding extracted refractive index was found to be ‘70.5, 133, and 149.5 GHz /RIU’, respectively. The polarization insensitivity and high perfect absorber from 00 to 900 for both “TE” and “TM” modes were exhibited, concluding that the proposed design is specifically viable for some important applications such as THz images, filtering, biological sensing, and optical communications.

Funding. Fundamental Research Funds for the Central Universities (2018gczd014, 20190038020050); Natural Science Foundation of Hunan Province (2018JJ2533); National Natural Science Foundation of China (61801521, 61971450).

Disclosures. The authors declared that they have no conflict of interest to this work.

Data availability. No new data were created or analyzed in this study. Data sharing is not applicable to this article.

References

1. S. Yoo, S. Lee, and Q.-H. Park, “Loss-free negative-index metamaterials using forward light scattering in dielectric meta-atoms,” *ACS Photonics* **5**(4), 1370–1374 (2018).
2. W. Cai, U. K. Chettiar, A. V. Kildishev, and V. M. Shalaev, “Optical cloaking with metamaterials,” *Nat. Photonics* **1**(4), 224–227 (2007).
3. D. Schurig, J. J. Mock, B. Justice, S. A. Cummer, J. B. Pendry, A. F. Starr, and D. R. Smith, “Metamaterial electromagnetic cloak at microwave frequencies,” *Science* **314**(5801), 977–980 (2006).
4. M. Manjappa, P. Pitchappa, N. Wang, C. Lee, and R. Singh, “Active control of resonant cloaking in a terahertz MEMS metamaterial,” *Adv. Opt. Mater.* **6**(16), 1800141 (2018).
5. Y. Liu, Y. Hao, K. Li, and S. Gong, “Radar cross section reduction of a microstrip antenna based on polarization conversion metamaterial,” *Antennas Wirel. Propag. Lett.* **15**, 80–83 (2016).

6. H. B. Baskey, E. Johari, and M. J. Akhtar, "Metamaterial structure integrated with a dielectric absorber for wideband reduction of antennas radar cross section," *IEEE Trans. Electromagn. Compat.* **59**(4), 1060–1069 (2017).
7. A. D. Tadesse, O. P. Acharya, and S. Sahu, "Application of metamaterials for performance enhancement of planar antennas: a review," *Int J RF Microw Comput Aided Eng* **30**(5), e22154 (2020).
8. Y. Cheng, Y. Nie, X. Wang, and R. Gong, "An ultrathin transparent metamaterial polarization transformer based on a twist-split-ring resonator," *Appl. Phys. A* **111**(1), 209–215 (2013).
9. N. K. Grady, J. E. Heyes, D. R. Chowdhury, Y. Zeng, M. T. Reiten, A. K. Azad, A. J. Taylor, D. A. Dalvit, and H.-T. Chen, "Terahertz metamaterials for linear polarization conversion and anomalous refraction," *Science* **340**(6138), 1304–1307 (2013).
10. S. H. Zainud-Deen, M. M. Badawy, and H. A. E.-A. Malhat, "Dielectric resonator antenna loaded with reconfigurable plasma metamaterial polarization converter," *Plasmonics* **14**(6), 1321–1328 (2019).
11. W. Xu, L. Xie, J. Zhu, X. Xu, Z. Ye, C. Wang, Y. Ma, and Y. Ying, "Gold nanoparticle-based terahertz metamaterial sensors: mechanisms and applications," *ACS Photonics* **3**(12), 2308–2314 (2016).
12. X. Hu, G. Xu, L. Wen, H. Wang, Y. Zhao, Y. Zhang, D. R. Cumming, and Q. Chen, "Metamaterial absorber integrated microfluidic terahertz sensors," *Laser Photonics Rev.* **10**(6), 962–969 (2016).
13. S. Khan and T. F. Eibert, "A multifunctional metamaterial-based dual-band isotropic frequency-selective surface," *IEEE Trans. Antennas Propag.* **66**(8), 4042–4051 (2018).
14. F. Yu, J. Wang, J. Wang, H. Ma, H. Du, Z. Xu, and S. Qu, "Reflective frequency selective surface based on low-permittivity dielectric metamaterials," *Appl. Phys. Lett.* **107**(21), 211906 (2015).
15. K. Chen, Y. Feng, L. Cui, J. Zhao, T. Jiang, and B. Zhu, "Dynamic control of asymmetric electromagnetic wave transmission by active chiral metamaterial," *Sci. Rep.* **7**(1), 1–10 (2017).
16. B.-X. Wang, L.-L. Wang, G.-Z. Wang, W.-Q. Huang, X.-F. Li, and X. Zhai, "Theoretical investigation of broadband and wide-angle terahertz metamaterial absorber," *IEEE Photonics Technol. Lett.* **26**(2), 111–114 (2014).
17. M. Diem, T. Koschny, and C. M. Soukoulis, "Wide-angle perfect absorber/thermal emitter in the terahertz regime," *Phys. Rev. B* **79**(3), 033101 (2009).
18. C. Arora, S. S. Pattnaik, and R. Baral, "Performance enhancement of patch antenna array for 5.8 GHz Wi-MAX applications using metamaterial inspired technique," *AEU-International Journal of Electronics and Communications* **79**, 124–131 (2017).
19. H. Hajian, A. Ghobadi, B. Butun, and E. Ozbay, "Active metamaterial nearly perfect light absorbers: a review," *JOSA B* **36**(8), F131–F143 (2019).
20. Y. Yuan, C. Dong, J. Gu, Q. Liu, J. Xu, C. Zhou, G. Song, W. Chen, L. Yao, and D. Zhang, "A scalable nickel–cellulose hybrid metamaterial with broadband light absorption for efficient solar distillation," *Adv. Mater.* **32**(17), 1907975 (2020).
21. H. Ou, F. Lu, Y. Liao, F. Zhu, and Y.-S. Lin, "Tunable terahertz metamaterial for high-efficiency switch application," *Results Phys.* **16**, 102897 (2020).
22. F. Qin, Z. Chen, X. Chen, Z. Yi, W. Yao, T. Duan, P. Wu, H. Yang, G. Li, and Y. Yi, "A tunable triple-band near-infrared metamaterial absorber based on Au nano-cuboids array," *Nanomaterials* **10**(2), 207 (2020).
23. D. Hu, T. Meng, H. Wang, and M. Fu, "Actively tunable dual-broadband graphene-based terahertz metamaterial absorber," *Chin. Phys. B* **30**(12), 126101 (2021).
24. Y. Ma, Q. Chen, J. Grant, S. C. Saha, A. Khalid, and D. R. Cumming, "A terahertz polarization insensitive dual band metamaterial absorber," *Opt. Lett.* **36**(6), 945–947 (2011).
25. Y. I. Abdulkarim, F. Ö. Alkurt, H. N. Awl, F. F. Muhammadsharif, M. Bakır, S. Dalgac, M. Karaaslan, and H. Luo, "An ultrathin and dual band metamaterial perfect absorber based on ZnSe for the polarization-independent in terahertz range," *Results Phys.* **26**, 104344 (2021).
26. P. Zamzam and P. Rezaei, "A terahertz dual-band metamaterial perfect absorber based on metal-dielectric-metal multi-layer columns," *Opt. Quantum Electron.* **53**(2), 109 (2021).
27. J. Grant, I. J. McCrindle, and D. R. Cumming, "Multi-spectral materials: hybridisation of optical plasmonic filters, a mid infrared metamaterial absorber and a terahertz metamaterial absorber," *Opt. Express* **24**(4), 3451–3463 (2016).
28. W. Meng, L. Que, J. Lv, L. Zhang, Y. Zhou, and Y. Jiang, "A triple-band terahertz metamaterial absorber based on buck Dirac semimetals," *Results Phys.* **14**, 102461 (2019).
29. B.-X. Wang, X. Zhai, G. Wang, W. Huang, and L. Wang, "Design of a four-band and polarization-insensitive terahertz metamaterial absorber," *IEEE Photonics J.* **7**, 1–8 (2014).
30. D. Chaurasiya, S. Ghosh, S. Bhattacharyya, and K. V. Srivastava, "An ultrathin quad-band polarization-insensitive wide-angle metamaterial absorber," *Microw. Opt. Technol. Lett.* **57**(3), 697–702 (2015).
31. T. Meng, D. Hu, and Q. Zhu, "Design of a five-band terahertz perfect metamaterial absorber using two resonators," *Opt. Commun.* **415**, 151–155 (2018).
32. I. E. Carranza, J. Grant, J. Gough, and D. R. Cumming, "Metamaterial-based terahertz imaging," *IEEE Trans. Terahertz Sci. Technol.* **5**(6), 892–901 (2015).
33. A. Tuniz, K. J. Kaltenecker, B. M. Fischer, M. Walther, S. C. Fleming, A. Argyros, and B. T. Kuhlmeier, "Metamaterial fibres for subdiffraction imaging and focusing at terahertz frequencies over optically long distances," *Nat. Commun.* **4**(1), 2706 (2013).

34. L. Yu, L. Hao, T. Meiqiong, H. Jiaoqi, L. Wei, D. Jinying, C. Xueping, F. Weiling, and Z. Yang, "The medical application of terahertz technology in non-invasive detection of cells and tissues: opportunities and challenges," *RSC Adv.* **9**(17), 9354–9363 (2019).
35. S. Poorgholam-Khanjari and F. B. Zarrabi, "Reconfigurable Vivaldi THz antenna based on graphene load as hyperbolic metamaterial for skin cancer spectroscopy," *Opt. Commun.* **480**, 126482 (2021).
36. J. Kim, K. Han, and J. W. Hahn, "Selective dual-band metamaterial perfect absorber for infrared stealth technology," *Sci. Rep.* **7**(1), 1–9 (2017).
37. H. Zou and Y. Cheng, "Design of a six-band terahertz metamaterial absorber for temperature sensing application," *Opt. Mater.* **88**, 674–679 (2019).
38. A. Mohanty, O. P. Acharya, B. Appasani, S. Mohapatra, and M. S. Khan, "Design of a Novel Terahertz Metamaterial Absorber for Sensing Applications," *IEEE Sens. J.* **21**(20), 22688–22694 (2021).
39. M. P. Hokmabadi, D. S. Wilbert, P. Kung, and S. M. Kim, "Design and analysis of perfect terahertz metamaterial absorber by a novel dynamic circuit model," *Opt. Express* **21**(14), 16455–16465 (2013).
40. Q. Xie, G. Dong, B.-X. Wang, and W.-Q. Huang, "Design of quad-band terahertz metamaterial absorber using a perforated rectangular resonator for sensing applications," *Nanoscale Res. Lett.* **13**(1), 1–8 (2018).
41. M. Baqir and S. Naqvi, "Electrically tunable terahertz metamaterial absorber comprised Cu/graphene strips," *Plasmonics* **15**(6), 2205–2211 (2020).
42. H. Zhu, Y. Zhang, L. Ye, Y. Li, Y. Xu, and R. Xu, "Switchable and tunable terahertz metamaterial absorber with broadband and multi-band absorption," *Opt. Express* **28**(26), 38626–38637 (2020).
43. G. Isić, B. Vasić, D. C. Zografopoulos, R. Beccherelli, and R. Gajić, "Electrically tunable critically coupled terahertz metamaterial absorber based on nematic liquid crystals," *Phys. Rev. Appl.* **3**(6), 064007 (2015).
44. P. Rufangura and C. Sabah, "Wide-band polarization independent perfect metamaterial absorber based on concentric rings topology for solar cells application," *J. Alloys Compd.* **680**, 473–479 (2016).
45. X. Chen, W. Fan, and C. Song, "Multiple plasmonic resonance excitations on graphene metamaterials for ultrasensitive terahertz sensing," *Carbon* **133**, 416–422 (2018).
46. C. Yuan, R. Yang, J. Wang, and J. Tian, "Tunable enhanced bandwidth all-graphene-dielectric terahertz metamaterial absorber/reflector," *Optik* **224**, 165517 (2020).
47. M. A. Cole, D. A. Powell, and I. V. Shadrivov, "Strong terahertz absorption in all-dielectric Huygens' metasurfaces," *Nanotechnology* **27**(42), 424003 (2016).
48. X. Huang, C. Lu, C. Rong, Z. Hu, and M. Liu, "Multiband ultrathin polarization-insensitive terahertz perfect absorbers with complementary metamaterial and resonator based on high-order electric and magnetic resonances," *IEEE Photonics J.* **10**, 1–11 (2018).
49. X. Cheng, R. Huang, J. Xu, and X. Xu, "Broadband terahertz near-perfect absorbers," *ACS Appl. Mater. Interfaces* **12**(29), 33352–33360 (2020).
50. T. Wang, L. Qu, L. Qu, Y. Zhang, H. Zhang, and M. Cao, "Tunable broadband terahertz metamaterial absorber using multi-layer black phosphorus and vanadium dioxide," *J. Phys. D: Appl. Phys.* **53**(14), 145105 (2020).
51. W. Pan, X. Yu, J. Zhang, and W. Zeng, "A broadband terahertz metamaterial absorber based on two circular split rings," *IEEE J. Quantum Electron.* **53**(1), 1–6 (2017).
52. B.-X. Wang, "Quad-band terahertz metamaterial absorber based on the combining of the dipole and quadrupole resonances of two SRRs," *IEEE J. Sel. Top. Quantum Electron.* **23**, 1–7 (2016).
53. B.-X. Wang, C. Tang, Q. Niu, Y. He, and T. Chen, "Design of narrow discrete distances of dual-/triple-band terahertz metamaterial absorbers," *Nanoscale Res. Lett.* **14**(1), 1–7 (2019).
54. R. Yahiaoui, S. Tan, L. Cong, R. Singh, F. Yan, and W. Zhang, "Multispectral terahertz sensing with highly flexible ultrathin metamaterial absorber," *J. Appl. Phys.* **118**(8), 083103 (2015).
55. A. S. Arezoomand, F. B. Zarrabi, S. Heydari, and N. P. Gandji, "Independent polarization and multi-band THz absorber base on Jerusalem cross," *Opt. Commun.* **352**, 121–126 (2015).
56. J. Wang, T. Lang, Z. Hong, M. Xiao, and J. Yu, "Design and fabrication of a triple-band terahertz metamaterial absorber," *Nanomaterials* **11**(5), 1110 (2021).
57. O. Ayop, M. K. Abd Rahim, N. A. Murad, N. A. Samsuri, and R. Dewan, "Triple band circular ring-shaped metamaterial absorber for x-band applications," *Prog. Electromagn. Res. M* **39**, 65–75 (2014).
58. S. Bhattacharyya, S. Ghosh, and K. V. Srivastava, "Equivalent circuit model of an ultra-thin polarization-independent triple band metamaterial absorber," *AIP Adv.* **4**(9), 097127 (2014).
59. G. Molero, C. Y. Tsai, C. Liu, H. J. Sue, S. Uenuma, K. Mayumi, and K. Ito, "Mechanical and scratch behaviors of polyrotaxane-modified poly (methyl methacrylate)," *J. Appl. Polym. Sci.* **138**(42), 51237 (2021).
60. S. Park and Y. Ahn, "Substrate effects on terahertz metamaterial resonances for various metal thicknesses," *J. Korean Phys. Soc.* **65**(11), 1843–1847 (2014).
61. H. Okamura, "A simple method for the Kramers-Kronig analysis of reflectance spectra measured with diamond anvil cell," in *Journal of Physics: Conference Series*, (IOP Publishing, 2012), 012013.
62. M. Ryu, S. H. Ng, V. Anand, S. Lundgaard, J. Hu, T. Katkus, D. Appadoo, Z. Vilagosh, A. W. Wood, and S. Juodkakis, "Attenuated total reflection at THz wavelengths: prospective use of total internal reflection and polariscopy," *Appl. Sci.* **11**(16), 7632 (2021).
63. O. Luukkonen, F. Costa, C. R. Simovski, A. Monorchio, and S. A. Tretyakov, "A thin electromagnetic absorber for wide incidence angles and both polarizations," *IEEE Trans. Antennas Propag.* **57**(10), 3119–3125 (2009).

64. S. Tretyakov, *Analytical Modeling in Applied Electromagnetics* (Artech House, 2003).
65. A. S. Saadeldin, M. F. O. Hameed, E. M. Elkaramany, and S. S. Obayya, "Highly sensitive terahertz metamaterial sensor," *IEEE Sens. J.* **19**(18), 7993–7999 (2019).
66. M. Islam, S. J. M. Rao, G. Kumar, B. P. Pal, and D. R. Chowdhury, "Role of resonance modes on terahertz metamaterials based thin film sensors," *Sci Rep* **7**(1), 1–8 (2017).